

# Preparation and Characterization of Undoped and Chromia-Doped Porous Alumina Using Different-Sized Particles

**Yen Ngoc Nguyen**

Hanoi University of Science and Technology

**Hai Minh Le**

Hanoi University of Science and Technology

**Makoto Nanko**

Nagaoka University of Technology

**Khanh Quoc Dang** (✉ [khanh.dangquoc@hust.edu.vn](mailto:khanh.dangquoc@hust.edu.vn))

School of Materials Science and Engineering <https://orcid.org/0000-0001-9416-891X>

---

## Research Article

**Keywords:** ceramic, dopant, sintering, combustion synthesis, porosity, strength

**Posted Date:** February 5th, 2021

**DOI:** <https://doi.org/10.21203/rs.3.rs-184866/v1>

**License:**  This work is licensed under a Creative Commons Attribution 4.0 International License.

[Read Full License](#)

---

# Abstract

Highly porous alumina ( $\text{Al}_2\text{O}_3$ ) was prepared by sintering of  $\text{Al}_2\text{O}_3$  powder using ammonia bicarbonate ( $\text{NH}_4\text{HCO}_3$ ) as a pore-forming agent and chromia ( $\text{Cr}_2\text{O}_3$ ) as a sintering additive. In order to investigate the influence of particle shape and size on the characterization of sintered porous  $\text{Al}_2\text{O}_3$ , the starting  $\text{Al}_2\text{O}_3$  powders included commercial disk micro-sized powder and synthesized spherical nanopowder. The nanoscale  $\text{Al}_2\text{O}_3$  powder was produced via combustion synthesis route. At the optimal pore-forming agent concentration, the porous  $\text{Al}_2\text{O}_3$  sintered by nanoparticles had a smaller pore size and a lower total porosity than the one prepared by microparticles. The differences of open porosity and closed porosity between porous  $\text{Al}_2\text{O}_3$  synthesized by micro and nano-scale powders with and without  $\text{Cr}_2\text{O}_3$  dopant were also discussed. In addition, the compressive strength of porous  $\text{Al}_2\text{O}_3$  achieved by nano-sized powders, especially with  $\text{Cr}_2\text{O}_3$  dopant, had a higher value in comparison with the one prepared by micro-sized powders.

## 1 Introduction

Porous materials have been utilized in a broad range of applications for both industrial and daily life sectors [1–5]. Among porous materials, porous ceramics possess many advantages over other porous materials such as polymers or metals, namely high hardness, chemical inertness, thermal shock resistance, corrosion and wear resistance, and low density [4–9]. Alumina ( $\text{Al}_2\text{O}_3$ ) has been one of the most common materials for applications of porous ceramics such as filters, catalysis, and thermal insulators [10–12]. It is well known that  $\text{Al}_2\text{O}_3$  enables the highest operating temperature, and additionally exhibits the good mechanical properties even at high porosity [13–17].

The challenges in the fabrication of macroporous ceramics are to tailor pore structure and mechanical strength. There are two typical types of pores, i.e. open pores and closed pores. While the open pores connect to the outside of the materials, the closed pores are individual and inaccessible. Porous materials used as filters and carriers require a highly open pore content, whereas those materials employed in sonic and thermal insulators require a highly closed pore content [18]. The porous fraction must be controlled in relation to the mechanical strength, since these properties are generally inversely related. One of the common strategies enhancing the strength of the highly porous  $\text{Al}_2\text{O}_3$  is to add sintering additives including chromia ( $\text{Cr}_2\text{O}_3$ ), titania ( $\text{TiO}_2$ ), magnesia ( $\text{MgO}$ ), calcium oxide ( $\text{CaO}$ ), etc. [19–21]. With a certain amount, these sintering additives reacts with  $\text{Al}_2\text{O}_3$  to create a solid solution or an intermediate phase on  $\text{Al}_2\text{O}_3$  particle surface, thus improves the sintering ability of  $\text{Al}_2\text{O}_3$  particles. Further, these additives can enhance the strength of bulk materials via dispersion strengthening or solid solution strengthening. Additionally, the mechanical strength of highly porous  $\text{Al}_2\text{O}_3$  has been tailored using ultrafine initial powders [22–24]. It is well documented that nanoparticles lead to the great densification of bulk materials due to their high specific surface area and induce excellent strength owing to the Hall-Petch strengthening.

For processing highly macroporous ceramics, sintering is an effective method combining with replica, sacrificial template, or direct foaming techniques [6, 25]. The sacrificial template method has been widely used due to its low-cost and simple process steps. This technique basically includes a dispersion of a sacrificial phase throughout the ceramic precursors, subsequently, compaction to form a green body, and finally decomposition of sacrificial agents to obtain the pores [25, 26]. The pore formers are commonly organic agents or salts such as wax spheres, naphthalene particles, poly methyl methacrylate, starch, NaCl, and ammonia bicarbonate ( $\text{NH}_4\text{HCO}_3$ ) [27–30]. The decomposition of pore formers may leave the undesired residual impurities in the final product, hence the selection of pore-forming agents and the decomposition process should be carefully controlled [26, 31]. Additionally, most of the pores achieved in the sacrificial template are open pores. Mohanta et.al [32] stated that highly porous alumina could be produced by mixing  $\text{Al}_2\text{O}_3$  powder with rice husk as a sacrificial agent, followed by uniaxial pressing to obtain the green compacts, and finally sintering at  $1700^\circ\text{C}$  for 2h. When the content of rice husk increased, the open porosity proportionally rose with the increase of total porosity. The total porosity could reach the maximum values of over 65% at 40% concentration of 75–180  $\mu\text{m}$ -sized rice husk, however, the open porosity was approximately equal to total porosity, i.e. up to 65%. At the total porosity of 65%, the porous materials exhibited a compressive strength of 9.18 MPa. In order to attain the closed pores, it has been reported that a slurry or solution of ceramic precursors and sacrificial agents should be formed [26, 33–36]. Porous alumina with high closed porosity was fabricated by gel-casting of  $\text{Al}_2\text{O}_3$  powder and polyethylene, subsequently sintering at  $1400^\circ\text{C}$  for 1h [37]. The closed porosity of bulk samples could reach a maximum of 43% when the total porosity was 62%. At the total porosity over 70%, the porous materials possessed a low compressive strength of 3.7 MPa.

In previous researches, porous  $\text{Al}_2\text{O}_3$  has been successfully prepared by sintering of micro-sized  $\text{Al}_2\text{O}_3$  powder using  $\text{NH}_4\text{HCO}_3$  as the pore former [38, 39]. The porosity of porous  $\text{Al}_2\text{O}_3$  could be controlled by adjusting the concentration of pore-forming agents, and most of pore structure was the open pores. Sintering additives including  $\text{Cr}_2\text{O}_3$  and  $\text{TiO}_2$  could significantly enhance the mechanical properties of porous  $\text{Al}_2\text{O}_3$ . However, the mechanical strength of highly porous  $\text{Al}_2\text{O}_3$  samples prepared with sintering additives was poor. Therefore, the objective of this study is to investigate the porous structure and mechanical strength of a highly porous  $\text{Al}_2\text{O}_3$  prepared from undoped and  $\text{Cr}_2\text{O}_3$ -doped  $\text{Al}_2\text{O}_3$  nanopowders. It was expected that nanoparticles could promote sinterability and enhance the mechanical strength of porous samples. Additionally, the content of open and closed porosities could be adjusted by initial powders and concentration of pore former without the usage of ceramic suspension.

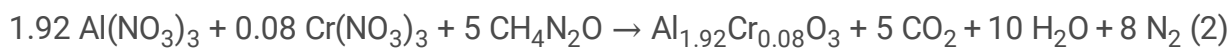
## 2 Materials And Method

The initial  $\text{Al}_2\text{O}_3$  powders without and with  $\text{Cr}_2\text{O}_3$  dopant with different particle shape and sizes were prepared in two following routes.

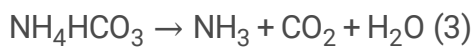
Route A: To attain the micro- $\text{Al}_2\text{O}_3$  and micro- $\text{Al}_2\text{O}_3/\text{Cr}$  powders, the starting materials were commercial  $\text{Al}_2\text{O}_3$  and  $\text{Cr}_2\text{O}_3$  powders (Sigma-Aldrich, Inc., Germany) with the purity of 99.5% and 99.9%, respectively.

The powder mixture of 99.5 wt.% Al<sub>2</sub>O<sub>3</sub> and 0.5 wt.% Cr<sub>2</sub>O<sub>3</sub> was ball-milled for 24h using Al<sub>2</sub>O<sub>3</sub> balls with ball powder mass ratios of 20/1 in a highly pure ethanol solution and then dried in a furnace at 120°C for 24h.

Route B: The nano-Al<sub>2</sub>O<sub>3</sub> and nano-Al<sub>2</sub>O<sub>3</sub>/Cr powders were synthesized via solution combustion method. The starting materials were Al(NO<sub>3</sub>)<sub>3</sub>·9H<sub>2</sub>O (99.99%, Sigma Aldrich, Germany) and Cr(NO<sub>3</sub>)<sub>3</sub>·6H<sub>2</sub>O (99.99%, Sigma Aldrich, Germany) as oxidizers and urea (CH<sub>4</sub>N<sub>2</sub>O, 99%, Sigma Aldrich, Germany) as a fuel. Each precursor was stoichiometrically balanced and then dissolved in distilled water. The aqueous solution was preheated at 500°C in an electric resistance furnace (Linn HT1300, Germany). The combustion reaction occurred according to the reactions (1) and (2) to form voluminous products. The combustion-synthesized product was de-agglomerated for 24h in a highly pure ethanol solution using Al<sub>2</sub>O<sub>3</sub> balls with ball-powder mass ratios of 20/1. The milled powder was dried at 120°C for 24h and then calcined at 1100°C for 2h.



The powders obtained through two routes were individually mixed with NH<sub>4</sub>HCO<sub>3</sub> content of 30 to 90 vol% by drying ball-mixing for 3h. The green bodies were formed by uniaxial pressing from powder mixture under a pressure of 300 MPa. The green pellets were annealed at 200°C for 2h to eliminate the pore former according to the reaction (3) and then at 500°C for 2h to remove the binders. Finally, the pellets were sintered in an electrical resistance furnace (HT1600, Linn, Germany) at 1550°C for 2h in an argon atmosphere.



The total porosity, open porosity and closed porosity of sintered pellets were measured using the Archimedes principle. The phase identification was implemented by X-ray diffraction (XRD, D5000 Siemens, Germany). The morphology of fractured surfaces was observed using the field emission scanning electron microscopy (FESEM, Hitachi S4800, Japan). The compressive strength was tested 10 times by a compressive strength tester (MTS 809, USA) as same as the standard compressive testing method specified in JIS-R 1608–2003 standard. The tested sample size was φ5mm x 12.5mm, and the load was applied gradually at a rate of 0.5mm/min.

### 3 Results And Discussion

The combustion-synthesized and commercial alumina powders without and with dopants were denoted as nano-Al<sub>2</sub>O<sub>3</sub>, nano-Al<sub>2</sub>O<sub>3</sub>/Cr, micro-Al<sub>2</sub>O<sub>3</sub>, and micro-Al<sub>2</sub>O<sub>3</sub>/Cr, respectively in the following part. XRD patterns of nano-Al<sub>2</sub>O<sub>3</sub> and nano-Al<sub>2</sub>O<sub>3</sub>/Cr powders before and after annealing at 1100°C for 2h are depicted in Fig. 1. Most reflections of α-Al<sub>2</sub>O<sub>3</sub> phase as being given in the ICDD 00-046-1212 file were

identified in combustion-synthesized powders. Although the phase transformation from  $\gamma$ - $\text{Al}_2\text{O}_3$  to  $\alpha$ - $\text{Al}_2\text{O}_3$  occurs at above  $1100^\circ\text{C}$  [40, 41], the combustion reaction could produce the  $\alpha$ - $\text{Al}_2\text{O}_3$  powder at the low pre-heat temperature of  $500^\circ\text{C}$ . The exothermicity of the reactions from the gaseous decomposition of reactants generated a large heat amount, thus a high temperature was achieved within a short duration. The flame temperature of the combustion reaction between  $\text{Al}(\text{NO}_3)_3$  and  $\text{CH}_4\text{N}_2\text{O}$  was observed and calculated at  $1550^\circ\text{C}$  and  $1427^\circ\text{C}$ , respectively [42]. Both observed and calculated flame temperatures were much higher than the temperature of  $\alpha$ - $\text{Al}_2\text{O}_3$  phase transformation. Hence, the synthesized powders contained only  $\alpha$ - $\text{Al}_2\text{O}_3$  phase, and no other forms of  $\text{Al}_2\text{O}_3$  were detected. Additionally, the broad  $\alpha$ - $\text{Al}_2\text{O}_3$  peaks in XRD patterns of combustion-synthesized powders indicate the low crystalline quality. After annealing, undoped and doped powders were also characterized by  $\alpha$ - $\text{Al}_2\text{O}_3$  peaks. The sharp and well-defined peak was attributed to the increase in crystallinity of  $\alpha$ - $\text{Al}_2\text{O}_3$  after annealing. There was no peak characterizing  $\text{Cr}_2\text{O}_3$  in the XRD pattern of doped  $\text{Al}_2\text{O}_3$  powders due to an extremely small amount of  $\text{Cr}_2\text{O}_3$ . Both the  $\alpha$ - $\text{Al}_2\text{O}_3$  and  $\text{Cr}_2\text{O}_3$  oxides have an identical hexagonal crystal structure that belongs to the trigonal  $\bar{R}3c$  space group. Consequently, the  $(\text{Al,Cr})_2\text{O}_3$  solid solution can be created according to the phase diagram of  $\text{Al}_2\text{O}_3/\text{Cr}_2\text{O}_3$ , and the formation of such solid solution was recognized at about  $1300^\circ\text{C}$  [43]. In experimental route A, the  $(\text{Al,Cr})_2\text{O}_3$  solid solution was generated owing to the diffusion between  $\text{Al}_2\text{O}_3$  and  $\text{Cr}_2\text{O}_3$  particles during sintering at  $1550^\circ\text{C}$ . For bottom-up approach in route B, the high flame temperature in combustion reaction induced the simultaneous formation of  $\alpha$ - $\text{Al}_2\text{O}_3$  and  $(\text{Al,Cr})_2\text{O}_3$  phases. The existence of such  $(\text{Al,Cr})_2\text{O}_3$  phase was not validated using XRD method due to their low fraction. However, the presence of the solid solution was observed through the color of the combustion-synthesized products. The white color of the synthesized  $\text{Al}_2\text{O}_3$  sample turned to a slightly pink color when  $\text{Cr}_2\text{O}_3$  was added. The change of the sample color agrees with the references [43, 44].

Figure 2 represents SEM images of commercial micro- $\text{Al}_2\text{O}_3$ , and annealed nano- $\text{Al}_2\text{O}_3$  and nano- $\text{Al}_2\text{O}_3/\text{Cr}$  powders. The commercial micro- $\text{Al}_2\text{O}_3$  particles had disk shape and average size from  $5\ \mu\text{m}$  to  $10\ \mu\text{m}$ . It was observed that the particle sizes were not difference between annealed nano- $\text{Al}_2\text{O}_3$  and nano- $\text{Al}_2\text{O}_3/\text{Cr}$  powders. The obtained nanoparticles possessed a uniform spherical shape, a size smaller than  $100\ \text{nm}$ , and narrow size distribution. However, the nano- $\text{Al}_2\text{O}_3$  powder was slightly agglomerated after annealing, while the nano- $\text{Al}_2\text{O}_3/\text{Cr}$  powder was well disaggregated.

The microstructure of the sintered  $\text{Al}_2\text{O}_3$  samples without pore formers is shown in Fig. 3. The grain shapes and sizes of the sintered micro- $\text{Al}_2\text{O}_3$  ceramic were similar to those of the starting powder, and the poor bonding was observed at the grain boundary. The grain size of nano- $\text{Al}_2\text{O}_3$  was well distributed within the submicron range and no local grain growth was identified. Beside the high specific surface area, the spherical shape of nanoparticles contributed to the uniform densification over the disk shape of microparticles. In both cases of nano- and micro-scale particles, the microstructure of  $\text{Cr}_2\text{O}_3$ -doped

samples revealed a higher grain growth than that of undoped ones, as the presence of solid solution  $(\text{Al,Cr})_2\text{O}_3$  on  $\text{Al}_2\text{O}_3$  particle surfaces enhanced the bonding ability at the grain boundary.

Figure 4 presents the porosities (i.e. total porosity, closed porosity, and open porosity) of porous  $\text{Al}_2\text{O}_3$  samples as a function of pore former concentrations. The total porosity of samples sintered from doped and/or nano-sized powders without pore former and with a fixed pore former concentration was much lower than that of undoped and/or micro-sized candidates (Fig. 4(a)). The micro- $\text{Al}_2\text{O}_3$  and micro- $\text{Al}_2\text{O}_3/\text{Cr}$  samples were totally collapsed after the process eliminating pore former at the pore former concentration of 30 vol% and 70 vol%, respectively. In contrast, the pore former concentration could go up to 90% in the case of nano- $\text{Al}_2\text{O}_3$  and nano- $\text{Al}_2\text{O}_3/\text{Cr}$  powders without collapse. The highest total porosity of the sintered samples corresponding to micro- $\text{Al}_2\text{O}_3/\text{Cr}$ , nano- $\text{Al}_2\text{O}_3$  and nano- $\text{Al}_2\text{O}_3/\text{Cr}$  were 78.3, 85.3, and 83.1%, respectively. The total porosity of micro- $\text{Al}_2\text{O}_3/\text{Cr}$  was 10–20 vol% higher than the  $\text{NH}_4\text{HCO}_3$  content due to the volume fraction of fine pores from partially sintering, whereas the total porosities of nano- $\text{Al}_2\text{O}_3$  and nano- $\text{Al}_2\text{O}_3/\text{Cr}$  were 10–20 vol% lower than the  $\text{NH}_4\text{HCO}_3$  amount due to the high shrinkage during sintering. The slope of total porosity - pore former concentration plots was smaller for the one of the micro- $\text{Al}_2\text{O}_3$  than for the one of the nano- $\text{Al}_2\text{O}_3$ . This indicated that the pore former was not effectively used for the pore formation in the micro- $\text{Al}_2\text{O}_3$ . For example, when the pore former was added by 50%, the increase in porosity compared to the ones without the pore former was approximately 20% for the micro- $\text{Al}_2\text{O}_3$  and approximately 35% for the nano- $\text{Al}_2\text{O}_3$ . It could be assumed that there was the collapse of the walls surrounding the pores in the case of micro- $\text{Al}_2\text{O}_3$  due to the poor densification.

When the pore former amount increased, the closed porosity tended to increase, then reach the maxima at the pore former concentration of 30% for micro- $\text{Al}_2\text{O}_3/\text{Cr}$  sample, and 50% for nano- $\text{Al}_2\text{O}_3$  ones, and subsequently decrease (Fig. 4(b)). The highest closed porosity in micro- $\text{Al}_2\text{O}_3/\text{Cr}$  was much lower than both nano- $\text{Al}_2\text{O}_3$  and nano- $\text{Al}_2\text{O}_3/\text{Cr}$ , and the maximum closed porosity in nano- $\text{Al}_2\text{O}_3/\text{Cr}$  was higher than nano- $\text{Al}_2\text{O}_3$ . The closed porosity as a percentage of total porosity was 24%, 48%, and 77% corresponding to micro- $\text{Al}_2\text{O}_3/\text{Cr}$ , nano- $\text{Al}_2\text{O}_3$  and nano- $\text{Al}_2\text{O}_3/\text{Cr}$ , respectively. In addition, the open porosity slightly increased when the pore former concentration increased up to the values, at which the closed porosity reached maxima (i.e. 30% for micro- $\text{Al}_2\text{O}_3/\text{Cr}$ , and 50% for nano- $\text{Al}_2\text{O}_3$  and nano- $\text{Al}_2\text{O}_3/\text{Cr}$ ). Subsequently, the open porosity sharply increased, and approximately equalled total porosity at maximum pore former concentration (i.e. 70% for micro- $\text{Al}_2\text{O}_3/\text{Cr}$ , and 90% for nano- $\text{Al}_2\text{O}_3$  and nano- $\text{Al}_2\text{O}_3/\text{Cr}$ ).

Figure 5 displays the microstructure of porous  $\text{Al}_2\text{O}_3$  prepared from different starting  $\text{Al}_2\text{O}_3$  powders with various pore former concentrations. The pores had irregular shape regardless of the initial  $\text{Al}_2\text{O}_3$  powders used. This unusual phenomenon may be caused by the  $\text{NH}_4\text{HCO}_3$  particle shape, the agglomeration of  $\text{NH}_4\text{HCO}_3$  particles during the powder mixing processes, the pressure increasing during pore former removal, or less shrinkage during sintering processes of the micro-sized powders. However, the pore size was changed with different size of  $\text{Al}_2\text{O}_3$  powders. In the case of 50% pore former, the pore size relating to nano- $\text{Al}_2\text{O}_3$  and nano- $\text{Al}_2\text{O}_3/\text{Cr}$  was much smaller than that of micro- $\text{Al}_2\text{O}_3/\text{Cr}$  due to the high

densification of nanoparticles. Pore quantity in nano- $\text{Al}_2\text{O}_3$  and nano- $\text{Al}_2\text{O}_3/\text{Cr}$  was mainly closed pores, while most of the pores in micro- $\text{Al}_2\text{O}_3/\text{Cr}$  were open pores. This agreed with the porosity data as mentioned before (Fig. 4b). When the amount of pore formers increased up to the maximum values, i.e. 70% for micro- $\text{Al}_2\text{O}_3/\text{Cr}$ , 90% for nano- $\text{Al}_2\text{O}_3$  and nano- $\text{Al}_2\text{O}_3/\text{Cr}$ , the large volume of  $\text{NH}_4\text{HCO}_3$  particles caused that pores were easier to connect to each other. Hence, the pore shape could not be observed in micro- $\text{Al}_2\text{O}_3/\text{Cr}$  and nano- $\text{Al}_2\text{O}_3$  cases at the maxima of pore forming agents, while pores in nano- $\text{Al}_2\text{O}_3/\text{Cr}$  could maintain a certain shape.

The microstructure of  $\text{NH}_4\text{HCO}_3$  pore-forming agents was observed by SEM with different magnification (Fig. 6(a),(b)). The particles of  $\text{NH}_4\text{HCO}_3$  had an irregular shape, hence the pore shape of porous samples was not also apparent. In high magnification, it is observed that the  $\text{NH}_4\text{HCO}_3$  particle was porous, this facilitated the complete decomposition process. The particle size of  $\text{NH}_4\text{HCO}_3$  and pore size of porous nano- $\text{Al}_2\text{O}_3$  and nano- $\text{Al}_2\text{O}_3/\text{Cr}$  with 50% pore former was measured 100 times based on SEM images, and subsequently depicted the size distribution in Fig. 6(c),(d),(e). The pore size distribution of nano- $\text{Al}_2\text{O}_3$  and nano- $\text{Al}_2\text{O}_3/\text{Cr}$  were similar to  $\text{NH}_4\text{HCO}_3$  particle size distribution, and there were no significant differences in the pore size range of porous samples achieved from nanopowders with and without  $\text{Cr}_2\text{O}_3$  dopant. Pore size ranges were less than 500  $\mu\text{m}$ , and most of the pore size concentrated on values less than 200  $\mu\text{m}$ .

Figure 7 shows the relationship between the porosity and the compressive strength of the sintered porous  $\text{Al}_2\text{O}_3$ . The porosity and the mechanical properties are inversely related, thus a higher content of the porosity of the bulk samples leads to the lower compressive strength. Nano- $\text{Al}_2\text{O}_3$  and nano- $\text{Al}_2\text{O}_3/\text{Cr}$  samples with porosity lower than 10% exhibited the excellent compressive strengths of 1275.5 and 1556.2 MPa, respectively. When the porosity increased up to 40%, the compressive strength was severely decreased lower than 200 MPa. At the same porosity of about 40%, the samples prepared from the micro- $\text{Al}_2\text{O}_3$ , micro- $\text{Al}_2\text{O}_3/\text{Cr}$ , nano- $\text{Al}_2\text{O}_3$ , and nano- $\text{Al}_2\text{O}_3/\text{Cr}$  exhibited the compressive strength of 66.2, 94.64, 124.7, and 142 MPa, respectively. The minimum values of compressive strength achieved by micro- $\text{Al}_2\text{O}_3/\text{Cr}$ , nano- $\text{Al}_2\text{O}_3$ , and nano- $\text{Al}_2\text{O}_3/\text{Cr}$  were approximately 4.15, 11.5, and 15.2 MPa, respectively when the total porosities reached about 80%. It was revealed that the porous ceramics fabricated from nano- $\text{Al}_2\text{O}_3/\text{Cr}$  powder exhibited a higher compressive strength than the other ones. When the total porosity was high over 80%, there was no significant difference between the compressive strength of nano- $\text{Al}_2\text{O}_3$  and nano- $\text{Al}_2\text{O}_3/\text{Cr}$ .

Both nanoparticles and  $\text{Cr}_2\text{O}_3$  dopant promote the densification of pore walls, hence aid in closing the pores in porous alumina. Therefore, porous ceramics prepared by nanoparticles possessed the smaller pore size and the lower total porosity; and could further exhibit the higher maximum closed porosity at the higher pore former concentration than ones sintered by the microparticles. The identical pore sizes and shapes between nano- $\text{Al}_2\text{O}_3$  and nano- $\text{Al}_2\text{O}_3/\text{Cr}$  were attributed to the good consolidation of pore walls; thus, the pore size represented the particle size of pore-forming agents. However, the existence of

$\text{Cr}_2\text{O}_3$  caused the increase in maximum closed porosity and maintained a certain pore shape in porous alumina having over 80% total porosity. Additionally, the nanoparticles induce the grain boundary strengthening in sintered bulk materials, while the  $\text{Cr}_2\text{O}_3$  dopant enhances the strength of materials via the solid solution strengthening. As a result, the alumina samples prepared by  $\text{Cr}_2\text{O}_3$ -doped nanoparticles had the lower total porosity and the higher compressive strength than the other ones at a low pore former concentration. Nevertheless,  $\text{Cr}_2\text{O}_3$  dopant did not have a significant effect on compressive strength at high total porosity, i.e. 80%.

## 4 Conclusion

The initial particle shape and size had an influence on the sintering ability, pore structures, and mechanical properties of the porous alumina fabricated through sintering combined with the sacrificial template method. Nanoparticles and  $\text{Cr}_2\text{O}_3$  dopant lead to a greater sintering rate and densification. Consequently, the porous alumina prepared from undoped and/or micro-sized powders possessed higher porosity than ones achieved from  $\text{Cr}_2\text{O}_3$ -doped and/or nano-sized powders at a fixed pore former concentration. The closed porosity varied with different starting  $\text{Al}_2\text{O}_3$  powders and reached the maximum up to 30% for nano- $\text{Al}_2\text{O}_3/\text{Cr}$  at 50% pore former. The porous alumina prepared from the nanoparticles had pore sizes smaller than those obtained from the micro- $\text{Al}_2\text{O}_3$  powders. In addition, nanoparticles and  $\text{Cr}_2\text{O}_3$  dopant enhanced the compressive strength of porous  $\text{Al}_2\text{O}_3$  samples. When the total porosity was over 80%, the compressive strength of highly porous alumina achieved by  $\text{Cr}_2\text{O}_3$ -doped fine initial powders could reach 15.2 MPa. The obtained results suggested that the proposed process could be efficiently used to tailor the pore structure and mechanical properties in porous  $\text{Al}_2\text{O}_3$  ceramics by changing the initial powders as well as the pore former quantity.

## References

- [1] Colombo P, Dunand DC, Kumar V. Porous materials: Less is more. *J Mater Res* 2013, **28**: 2187- 2190.
- [2] Li F, Huang X, Liu JX, *et al.* Sol-gel derived porous ultra-high temperature ceramics. *J Adv Ceram* 2020, **9**: 1-16.
- [3] Yan S, Pan Y, Wang L, *et al.* Synthesis of low-cost porous ceramic microspheres from waste gangue for dye adsorption. *J Adv Ceram* 2018, **7**:30–40.
- [4] Wu JM, Zhang XY, Xu J, *et al.* Preparation of porous  $\text{Si}_3\text{N}_4$  ceramics via tailoring solid loading of  $\text{Si}_3\text{N}_4$  slurry and  $\text{Si}_3\text{N}_4$  poly-hollow microsphere content. *J Adv Ceram* 2015, **4**:260–266.
- [5] Xiong Y, Tang Z, Wang Y, *et al.* Gas sensing capabilities of  $\text{TiO}_2$  porous nanoceramics prepared through premature sintering. *J Adv Ceram* 2015, **4**: 152-157.

- [6] Hammel EC, Ighodaro OLR, Okoli OI. Processing and properties of advanced porous ceramics: An application based review. *Ceram Int* 2004, **40**: 15351-15370.
- [7] Ohji T, Fukushima M. Macro-porous ceramics: Processing and properties. *Int Mater Rev* 2012, **57**: 115-131.
- [8] Guzman IY. Certain principles of formation of porous ceramic structures. Properties and application. *Glass Ceram* 2003, **60**: 280-283.
- [9] Li D, Li M. Porous  $Y_2SiO_5$  ceramic with low thermal conductivity. *J Mater Sci Technol* 2012, **28**: 799-802.
- [10] Wu JM, Chen Y, Zhang XY, *et al.* Phase evolution and properties of novel  $Al_2O_3$ -based poly-hollow microsphere (PHM) ceramics. *J Adv Ceram* 2016, **5**:176–182.
- [11] Liu J, Huo W, Zhang X, *et al.* Optimal design on the high-temperature mechanical properties of porous alumina ceramics based on fractal dimension analysis. *J Adv Ceram* 2018, **7**:89–98.
- [12] Tsuruki Y, Sakai M, Isobe T, *et al.* Static and dynamic hydrophobicity of alumina-based porous ceramics impregnated with fluorinated oil. *J Mater Res* 2014, **29**: 1546-1555.
- [13] Shimizu T, Matsuura K, Furue H, *et al.* Thermal conductivity of high porosity alumina refractory bricks made by a slurry gelation and foaming method. *J Eur Ceram Soc* 2013, **33**: 3429-3435.
- [14] Isobe T, Kameshima Y, Nakajima A, *et al.* Gas permeability and mechanical properties of porous alumina ceramics with unidirectionally aligned pores. *J Eur Ceram Soc* 2007, **27**: 53-59.
- [15] Chen X, Du J, Gan G, *et al.* Effect of solid content on performance of porous alumina ceramic by gel-foaming. *Adv Mater Res* 2012, **476-478**: 1007-1010.
- [16] Gregorová E, Pabst W, Živcová Z, *et al.* Porous alumina ceramics prepared with wheat flour. *J Eur Ceram Soc* 2010, **30**: 2871-2880.
- [17] Colonetti VC, Sanches MF, de Souza VC, *et al.* Cellular ceramics obtained by a combination of direct foaming of soybean oil emulsified alumina suspensions with gel consolidation using gelatin. *Ceram Int* 2018, **44**: 2436-2445.
- [18] Ishizaki K, Komarneni S, Nanko M. *Porous Materials: Process, Technology and Applications*. Kluwer Academic, 1998.
- [19] Prabhakaran K, Melkeri A, Gokhale NM, *et al.* Preparation of macroporous alumina ceramics using wheat particles as gelling and pore forming agent. *Ceram Int* 2007, **33**: 77-81.

- [20] Cutler IB, Bradshaw C, Christensen CJ, *et al.* Sintering of alumina at temperatures of 1400°C and below. *J Am Ceram Soc* 1957, **40**: 134-139.
- [21] Harun Z, Ismail NF, Badarulzaman NA. Effect of MgO additive on microstructure of Al<sub>2</sub>O<sub>3</sub>. *Adv Mater Res* 2012, **488-489**: 335-339.
- [22] Behera PS, Sarkar R, Bhattacharyya S. Nano alumina: A review of the powder synthesis method. *Interceram – Int Ceram Rev* 2016, **65**: 10-16.
- [23] Rajendran S. Production of ultrafine alpha alumina powders and fabrication of fine-grained strong ceramics. *J Mater Sci* 1994, **29**: 5664-5672.
- [24] Krell A, Blank P. Grain size dependence of hardness in dense submicrometer alumina. *J Am Ceram Soc* 1995, **78**: 1118-1120.
- [25] Studart AR, Gonzenbach UT, Tervoort EJ, *et al.* Processing routes to macroporous ceramics: A review. *J Am Ceram Soc* 2006, **89**: 1771-1789.
- [26] Vakifahmetoglu C, Semerci T, Soraru GD. Closed porosity ceramics and glasses. *J Am Ceram Soc* 2020, **103**: 2941-2969.
- [27] Chevalier E, Chulia D, Pouget C, *et al.* Fabrication of porous substrates: A review of processes using pore forming agents in the biomaterial field. *J Pharm Sci* 2008, **97**: 1135-1154.
- [28] Xue LA, Chen IW. Low-temperature sintering of alumina with liquid-forming additives. *J Am Ceram Soc* 1991, **74**: 2011-2013.
- [29] Zivcová Z, Gregorová E, Pabst W. Alumina ceramics prepared with new pore-forming agents. *Process Appl Ceram* 2008, **2**: 1-8.
- [30] Wang YQ, Tao J, Zhang JJ, *et al.* Effects of addition of NH<sub>4</sub>HCO<sub>3</sub> on pore characteristics and compressive properties of porous Ti-10%Mg composites. *Trans Nonferr Met Soc China* 2011, **21**: 1074-1079.
- [31] Ali MS, Hanim MAA, Tahir SM, *et al.* Preparation and characterization of porous alumina ceramics using different pore agents. *J Ceram Soc Japan* 2017, **125**: 402-412.
- [32] Mohanta K, Kumar A, Parkash O, *et al.* Low cost porous alumina with tailored microstructure and thermal conductivity prepared using rice husk and sucrose. *J Am Ceram Soc* 2014, **97**: 1708-1719.
- [33] Kim YW, Kim SH, Kim HD, *et al.* Processing of closed-cell silicon oxycarbide foams from a preceramic polymer. *J Mater Sci* 2004, **39**: 5647-5652.

- [34] Devavarapu S, Chaudhuri P, Shrivastava A, *et al.* Processing of porous alumina by foaming method-effect of foaming agent, solid loading and binder. *Ceram Int* 2019, **45**: 12264-12273.
- [35] Kim YW, Jin YJ, Chun YS, *et al.* A simple pressing route to closed-cell microcellular ceramics. *Scr Mater* 2005, **53**: 921-925.
- [36] Bakkar S, Lee J, Ku N, *et al.* Design of porous aluminum oxide ceramics using magnetic field-assisted freeze-casting. *J Mater Res* 2020, **35**: 2859-2869.
- [37] Tulliani JM, Lombardi M, Palmero P, *et al.* Development and mechanical characterization of novel ceramic foams fabricated by gel-casting. *J Eur Ceram Soc* 2013, **33**: 1567-1576.
- [38] Le HM, Nguyen DM, Dang KQ. Influence of sintering additives on the porous structure and mechanical properties of porous alumina. *J Sci Technol Tech Univ* 2017, **119**: 71-75.
- [39] Le HM, Nguyen DM, Dang KQ. Synthesis of highly porous alumina via powder metallurgy method using TiO<sub>2</sub> as sintering additive. *J Sci Technol Tech Univ* 2018, **124**: 57-62.
- [40] Macêdo MIF, Bertran CA, Osawa CC. Kinetics of the  $\gamma \rightarrow \alpha$ -alumina phase transformation by quantitative X-ray diffraction. *J Mater Sci* 2007, **42**: 2830-2936.
- [41] Bodaghi M, Mirhabibi AR, Zolfonun H, *et al.* Investigation of phase transition of  $\gamma$ -alumina to  $\alpha$ -alumina via mechanical milling method. *Ph Transit* 2008, **81**: 571-580.
- [42] Patil KC, Hegde MS, Rattan T, *et al.* *Chemistry of Nanocrystalline Oxide Materials: Combustion Synthesis, Properties and Applications*. Singapore: World Scientific, 2008.
- [43] Bondioli F, Ferrari AM, Leonelli C, *et al.* Reaction mechanism in alumina/chromia (Al<sub>2</sub>O<sub>3</sub>-Cr<sub>2</sub>O<sub>3</sub>) solid solutions obtained by coprecipitation. *J Am Ceram Soc* 2000, **83**: 2036-2040.
- [44] Dang KQ, Nanko M. Effects of pressure and temperature on sintering of Cr-doped Al<sub>2</sub>O<sub>3</sub> by pulsed electric current sintering process. *IOP Conf Ser Mater Sci Eng* 2011, **20**: 012004.

## Figures

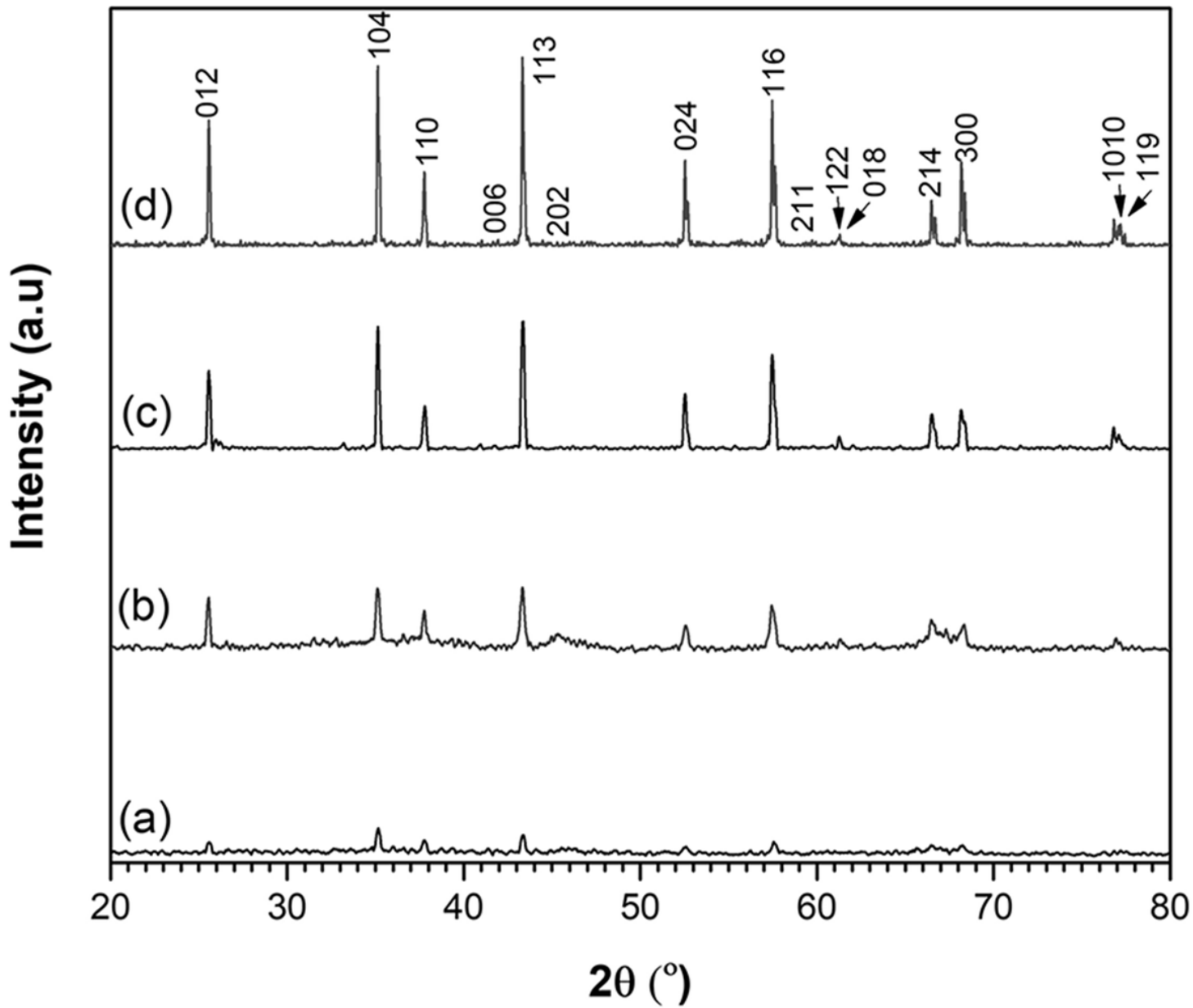
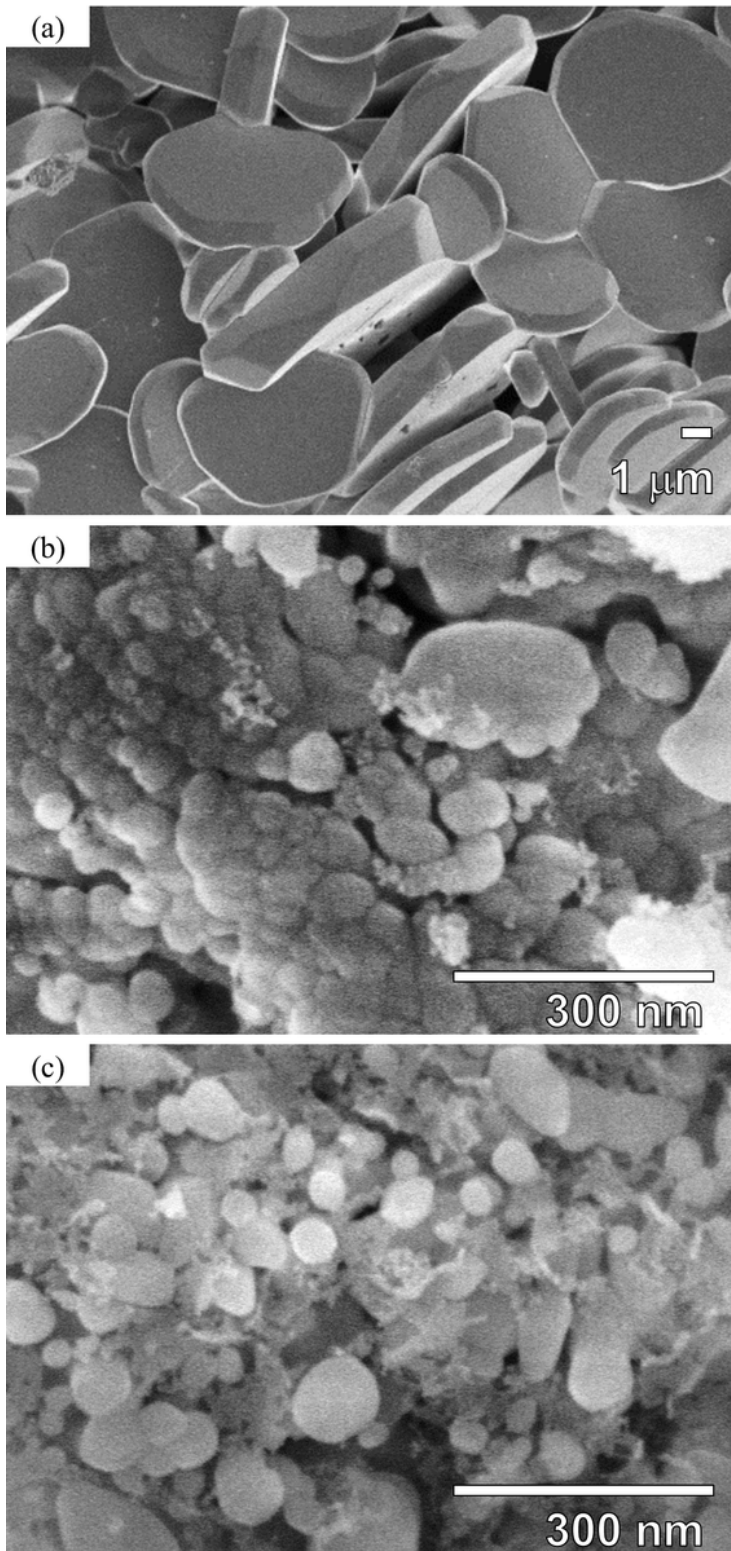


Figure 1

XRD patterns of (a) nano-Al<sub>2</sub>O<sub>3</sub> and (b) nano-Al<sub>2</sub>O<sub>3</sub>/Cr; and annealed (c) nano-Al<sub>2</sub>O<sub>3</sub> and (d) nano-Al<sub>2</sub>O<sub>3</sub>/Cr powders



**Figure 2**

SEM images of (a) commercial micro-Al<sub>2</sub>O<sub>3</sub>, annealed (b) nano-Al<sub>2</sub>O<sub>3</sub> and (c) nano-Al<sub>2</sub>O<sub>3</sub>/Cr powders

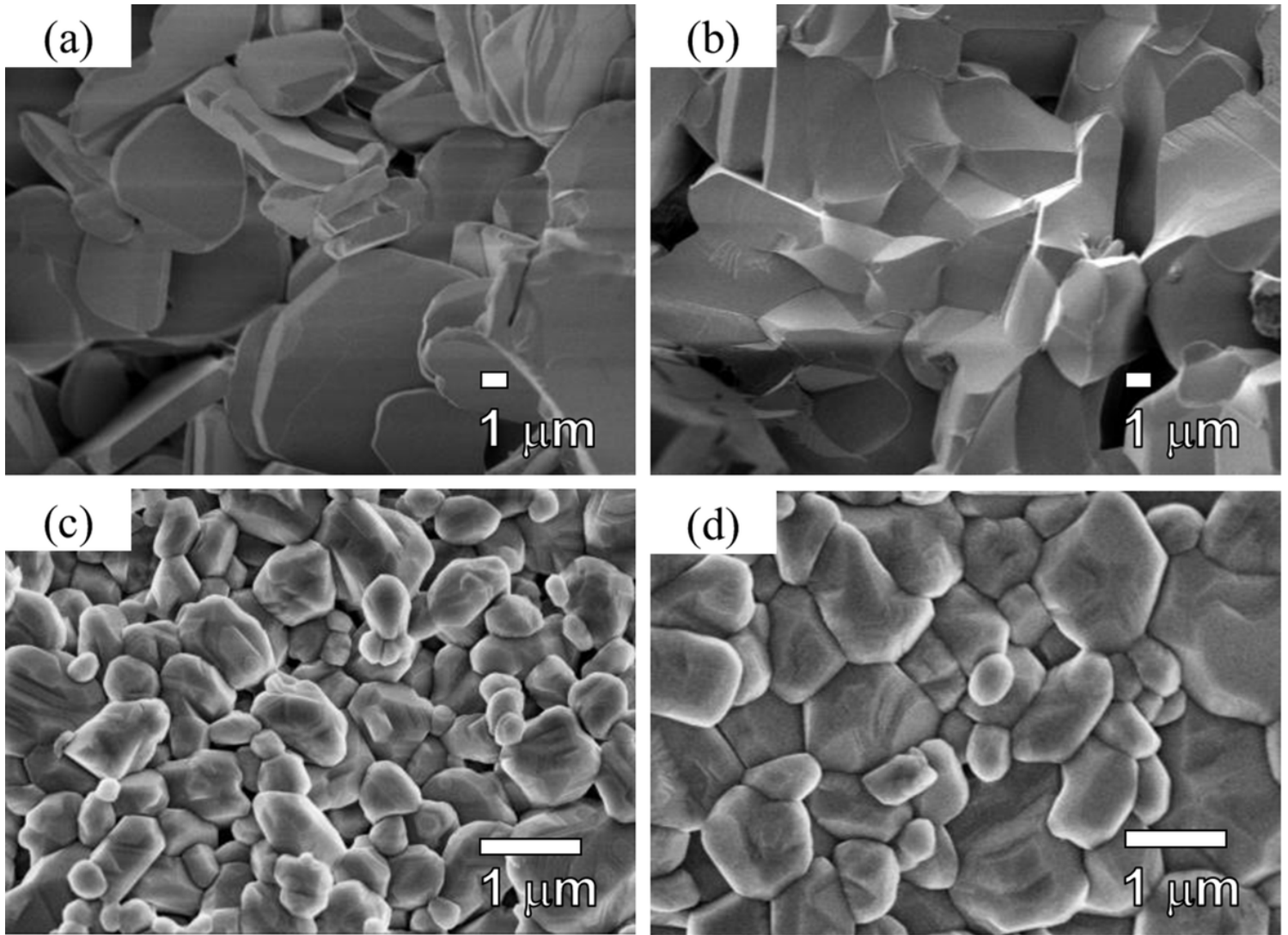


**Figure 3**

SEM images of Al<sub>2</sub>O<sub>3</sub> samples sintered by (a) micro-Al<sub>2</sub>O<sub>3</sub>, (b) micro-Al<sub>2</sub>O<sub>3</sub>/Cr, (c) nano-Al<sub>2</sub>O<sub>3</sub> and (d) nano-Al<sub>2</sub>O<sub>3</sub>/Cr powders

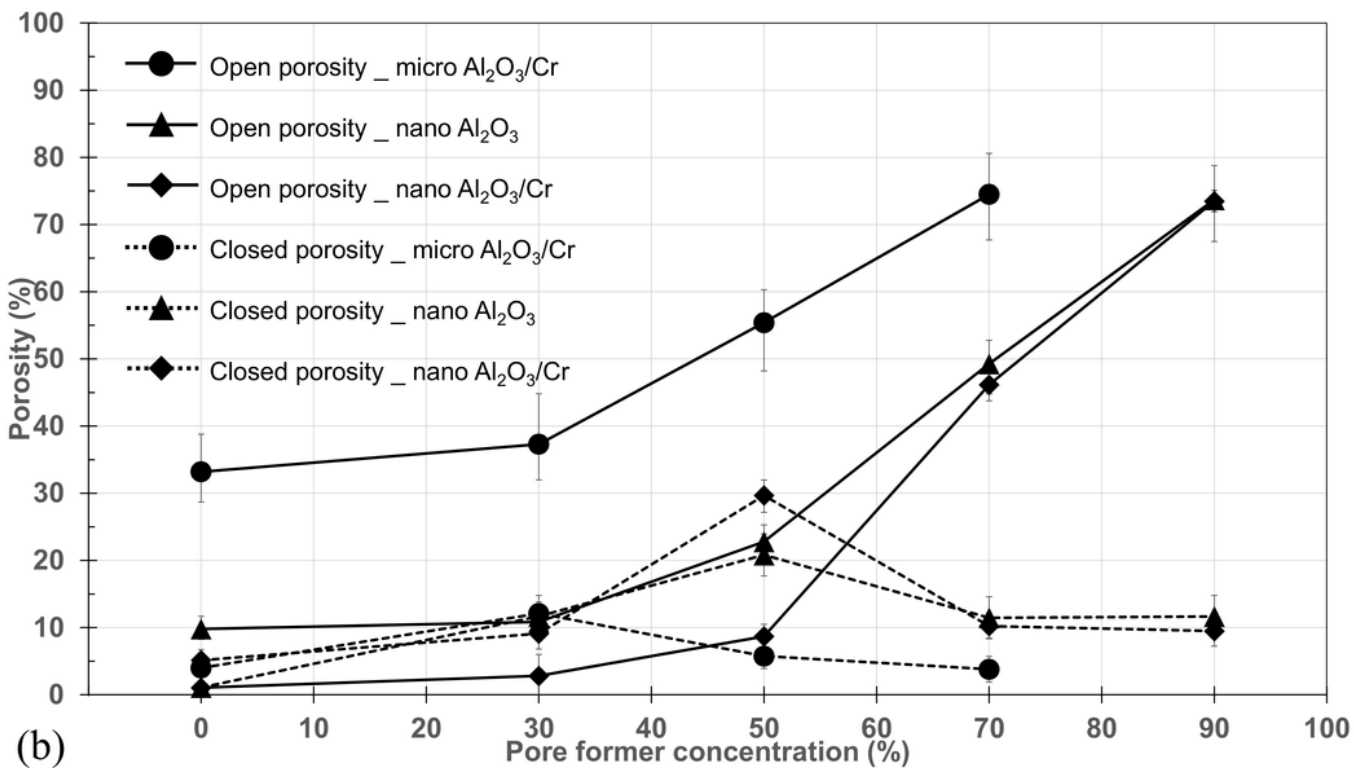
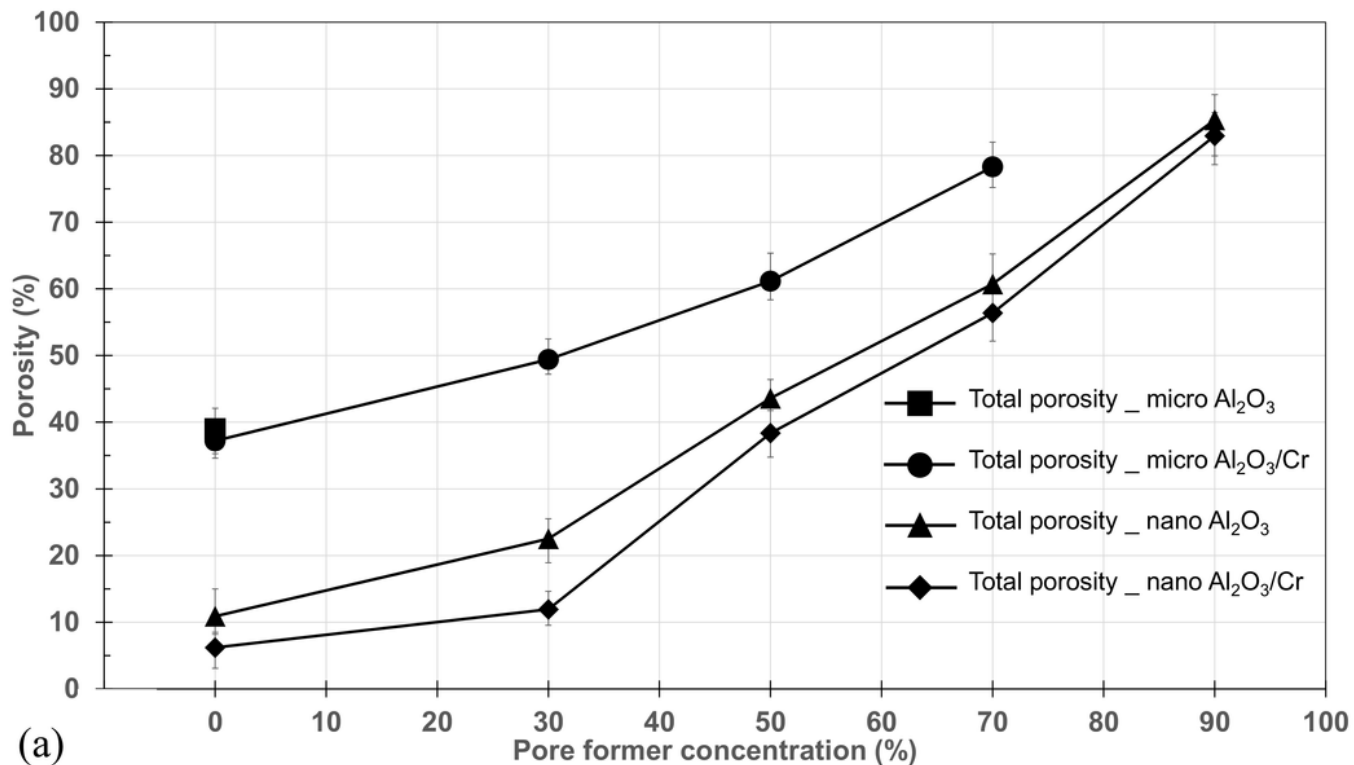


**Figure 4**

Evolution of the (a) total porosity, (b) open and closed porosities as a function of the pore former concentration

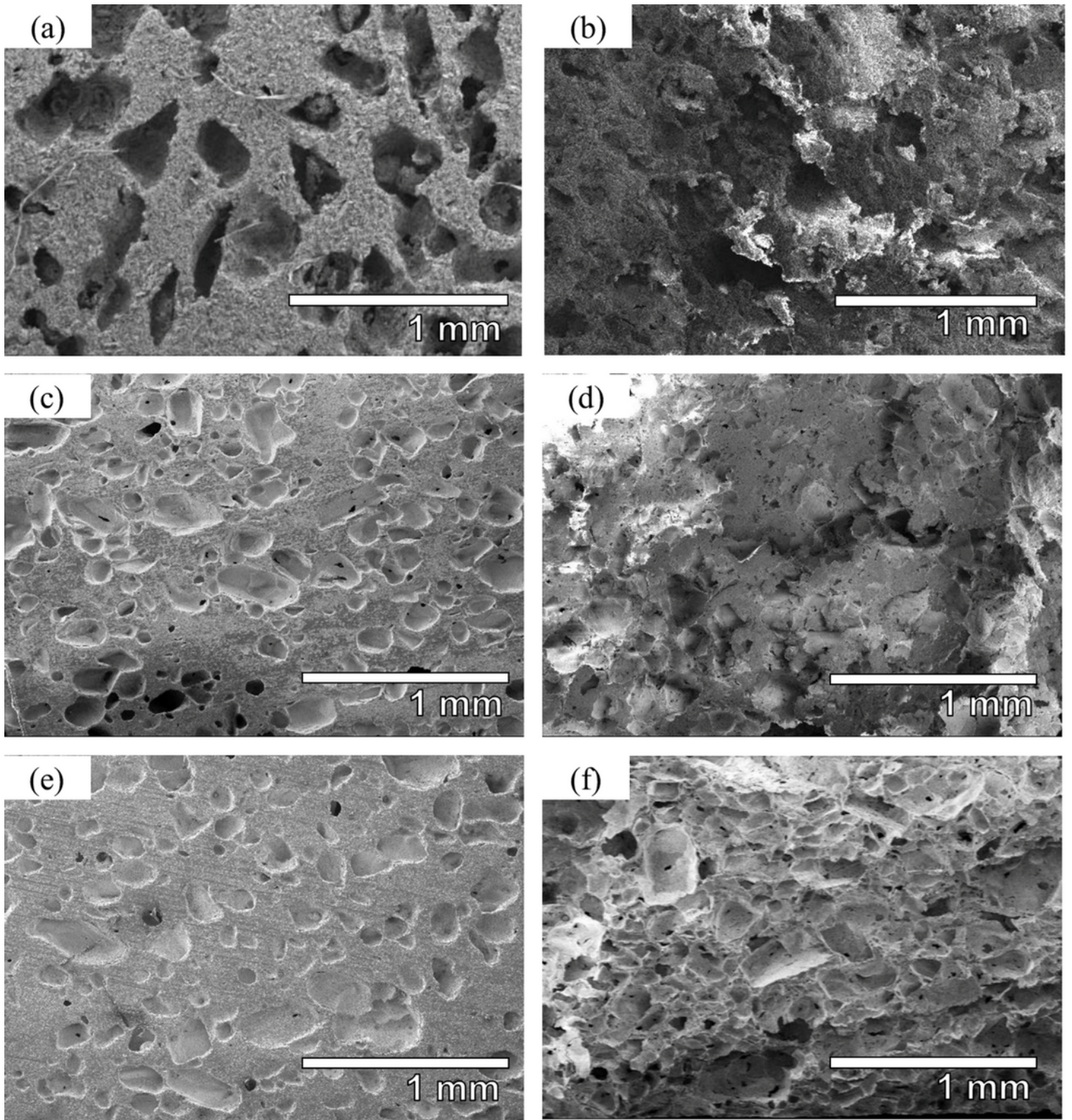


**Figure 5**

Microstructure of porous  $\text{Al}_2\text{O}_3$  bulk samples prepared from micro- $\text{Al}_2\text{O}_3/\text{Cr}$ , nano- $\text{Al}_2\text{O}_3$ , and nano- $\text{Al}_2\text{O}_3/\text{Cr}$  with (a), (c), (e) 50%, and (b), (d), (f) 90% pore former, respectively

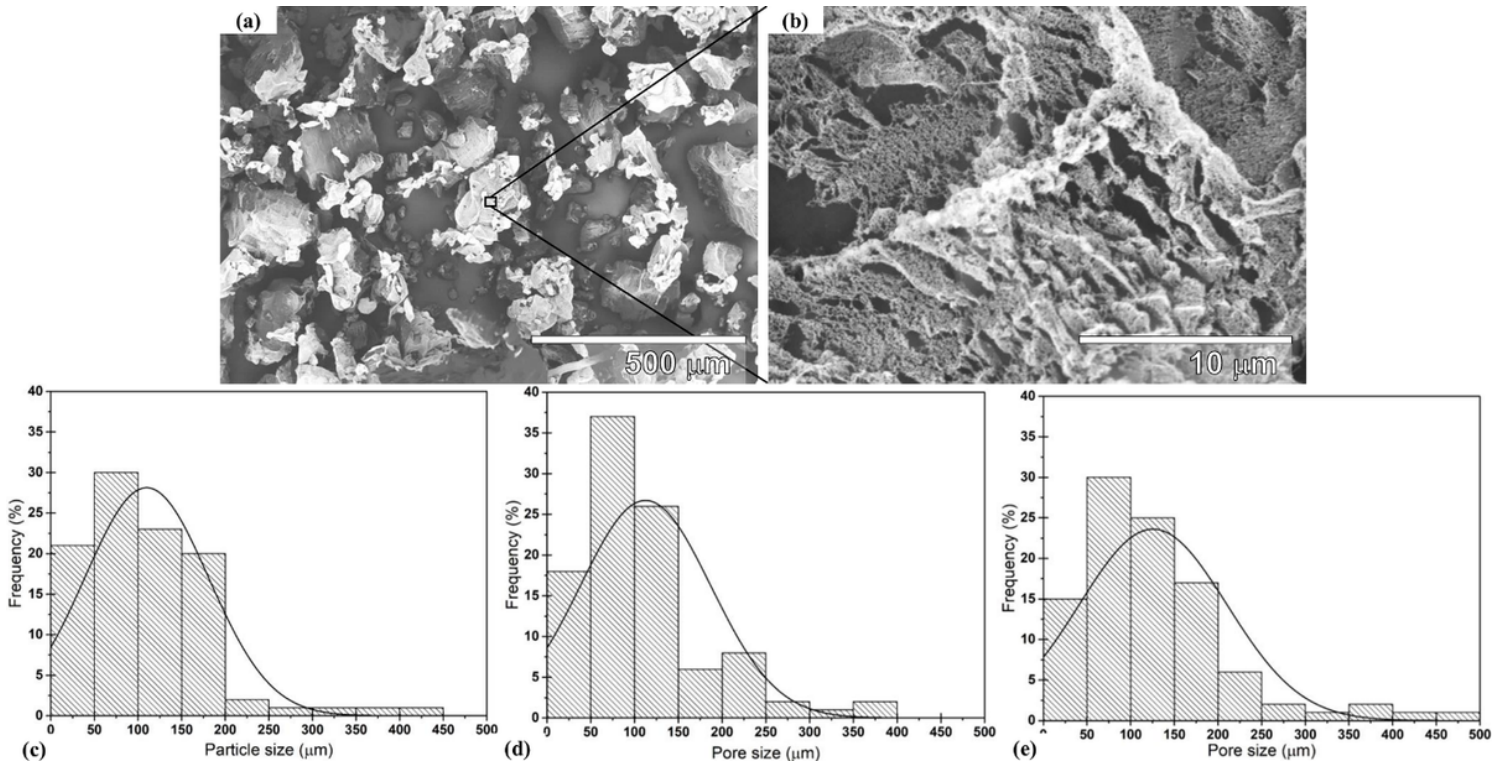


**Figure 6**

Microstructure of  $\text{NH}_4\text{HCO}_3$  pore former with different magnification ((a) x100, and (b) x5,000); (c)  $\text{NH}_4\text{HCO}_3$  particle size distribution; and pore size distribution of porous (d) nano- $\text{Al}_2\text{O}_3$  and (e) nano- $\text{Al}_2\text{O}_3/\text{Cr}$  with 50% pore former

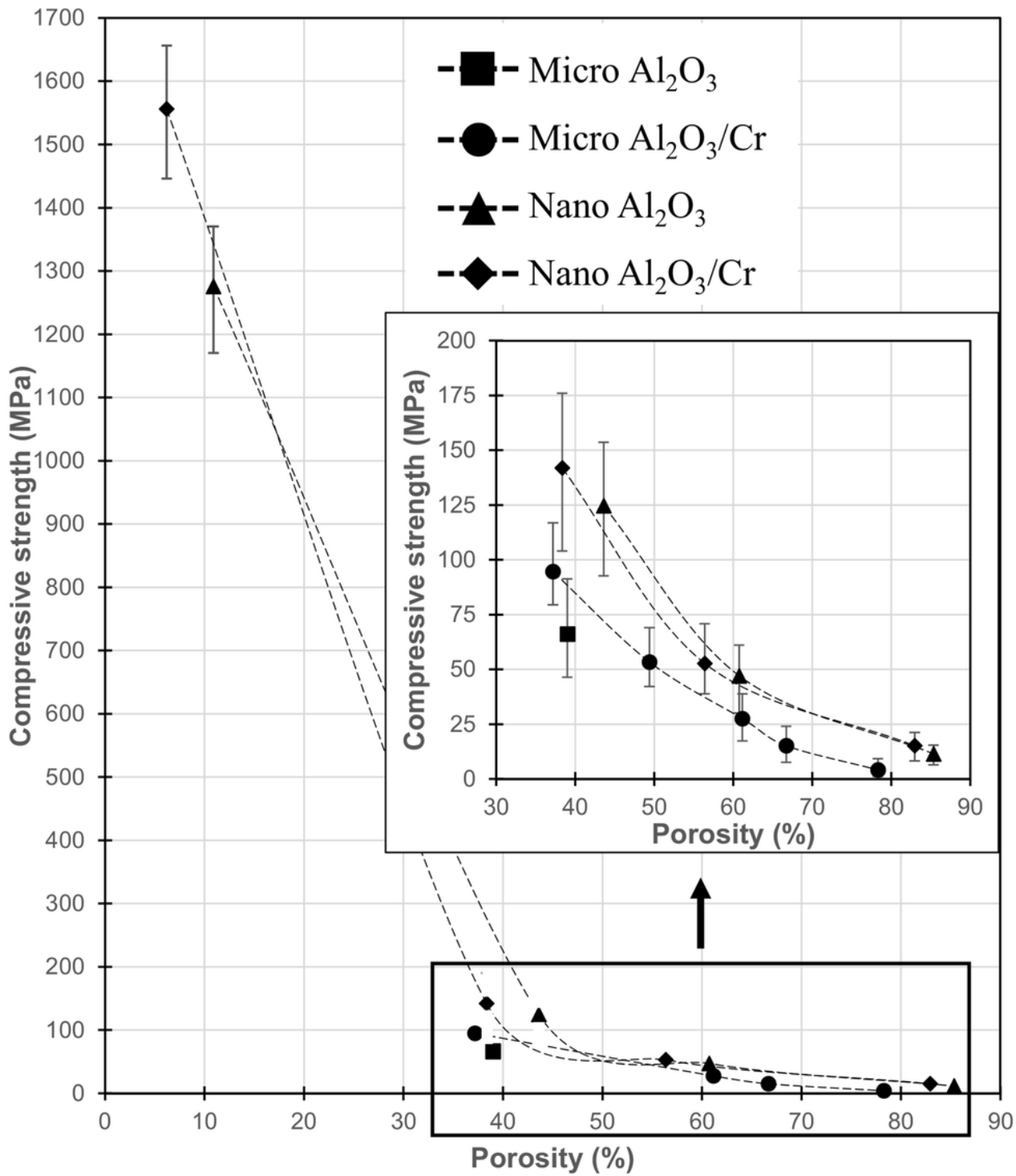


Figure 7

Relationship between porosity and compressive strength of porous Al<sub>2</sub>O<sub>3</sub>